Generic Rotating-Frame-Based Approach to Chaos Generation in Nonlinear Micro- and Nanoelectromechanical System Resonators

Samer Houri,* Motoki Asano, and Hiroshi Yamaguchi
NTT Basic Research Laboratories, NTT Corporation, 3-1 Morinosato-Wakamiya, Atsugi-shi, Kanagawa 243-0198, Japan

Natsue Yoshimura, Yasuharu Koike, and Ludovico Minati†
Institute of Innovative Research, Tokyo Institute of Technology, Yokohama 226-8503, Japan

(Received 26 February 2020; revised 26 July 2020; accepted 9 September 2020; published 23 October 2020)

This Letter provides a low-power method for chaos generation that is generally applicable to nonlinear micro- and nanoelectromechanical systems (MNEMS) resonators. The approach taken is independent of the material, scale, design, and actuation of the device in question; it simply assumes a good quality factor and a Duffing type nonlinearity, features that are commonplace to MNEMS resonators. The approach models the rotating-frame dynamics to analytically constrain the parameter space required for chaos generation. By leveraging these common properties of MNEMS devices, a period-doubling route to chaos is generated using smaller forcing than typically reported in the literature.

DOI: 10.1103/PhysRevLett.125.174301

Chaotic dynamics have received interest owing to their extraordinary ability to generate complex behaviors, such as synchronization patterns, even in simple and fixed arrangements of coupled nodes. Countless applications have been discussed, spanning control systems, telecommunications and neuroscience [1–4]. Recently, the field has witnessed a resurgence of interest due to the possibility of building large-scale hardware reservoirs from coupled nonlinear oscillators. To meet the requirements for practical application, high-integration and low-power implementations are necessary [5,6].

Micro- and nanoelectromechanical systems (MNEMS) provide experimental platforms for investigating and generating such dynamics, as they are easily amenable to very large-scale integration, low-power operation, and they inherently exhibit rich nonlinear behavior [7,8]. Indeed, chaos generation is well reported in the MNEMS scientific literature [9–19].

However, chaos generation reported in the literature for MNEMS devices resorts to nongeneral properties, e.g., nonsmooth nonlinearity [12], a high number of phase space dimensions ($n > 3$) obtained via interdevice or intermodal coupling [9–11], or extreme nonlinearity by operating near the electrostatic pull in [14,15]. A widespread approach is based on the creation of a static double-well potential either through electrostatic forces or by using buckled structures [16–18,20]. None of these approaches hinges around a common denominator property: they are, therefore, not transferable to nonlinear MNEMS resonators in general. In fact, they commonly require a large actuation voltage, thus negating one of the main appeals of MNEMS devices [12,14–18].

An interesting case is that of the static double-well potential, which is described by a Duffing equation (a system possessing a cubic nonlinearity [21]) where the linear component is negative and the cubic component is positive. Period-doubling bifurcations and chaos in such systems have been studied [22] and been subject to experimental investigations [23–25]. While such systems can be reproduced in MNEMS devices [16–18,20], nearly all MNEMS devices inherently exhibit a different type of cubic nonlinearity [26], equally captured by a variant of the Duffing equation, whereby the linear component is positive and the cubic component can be either positive or negative. Such MNEMS resonators can exhibit dynamic bistability [27,28].

In contrast to the static double-well systems, which can only be created through the use of specific materials or designs [14–18,29,30], the approach presented here relies on the dynamically generated double-well pseudopotential that is created when a generic nonlinear Duffing resonator is driven into the bistable regime [27]. Since bistability is accessed when the resonator's vibration amplitude is on the same order as some scaling parameter (e.g., thickness [26]), such pseudopotentials can be generated and manipulated by changing the drive conditions without requiring device or setup redesign.

The main purpose of this Letter is to demonstrate chaos generation in a perturbed "dynamic double well" in a manner that parallels chaos generation in driven "static double-well" systems, albeit with significantly lower drive amplitudes. Thus, two narrowly spaced drive tones are applied to the system, whereby the first creates the "dynamic double well" and the second perturbs it [31].

Since the displacement of the MNEMS resonator studied herein is moderate, i.e., on the order of the structural thickness, then a perturbation-based approach to analyze the dynamics is justified [27,32–34]. To represent the underlying dynamics we employ the rotating frame approximation (RFA), whereby a slow flow (a time-varying envelope) dynamics is overlaid on top of an otherwise purely sinusoidal response, and the timescales (τ) associated with this slow flow are on the order of the resonator linewidth (γ), i.e., $\tau \approx \mathcal{O}(1/\gamma)$ [27,32].

When a Duffing resonator is driven near resonance, its steady-state response as seen in the RFA corresponds to a fixed point in the phase space; in case the resonator is driven into the bistable regime, the response shows two distinct stable fixed points and a saddle point [33]. This latter configuration implies that homoclinic connections (i.e., trajectories that start and end in the saddle point and orbit one of the stable fixed points) may exist in the RFA phase space of a Duffing resonator. Thus, just as a "static double-well" potential provides homoclinic connections in the rest frame, so does the dynamic Duffing bistability provide homoclinic connections in the rotating frame, and it is the perturbation of such homoclinics that is responsible for the generation of chaos [22,24,35]. It can be further shown that compared to the static double well, the use of the dynamic bistability brings amplitude gains that are on the order of $\sqrt{Q}$ (see the Supplemental Material [36]).

This argument can be demonstrated by considering the Duffing equation for a two tone-driven MNEMS resonator, given as [27]

$$\ddot{x} + \gamma\dot{x} + \omega_0^2 x + \alpha x^3 = \eta F_1 \cos(\omega_1 t) + \eta F_2 \cos(\omega_2 t), \quad (1)$$

where x is the displacement, and γ, ω_0, α are, respectively, the damping, natural frequency, and Duffing nonlinearity of the resonator. F_1, F_2, ω_1, and ω_2 are the amplitudes and frequencies of two externally applied driving forces, and η is the transduction coefficient. We introduce dimensionless constants as $\bar{t} = t \times \omega_0$, $\bar{\gamma} = \gamma/\omega_0$, $\bar{\alpha} = \alpha/\omega_0^2$, $\bar{F}_1 = \eta F_1/\omega_0^2$, and $\bar{F}_2 = \eta F_2/\omega_0^2$. Hereon, all equations are written using this form, however, the bars are dropped for convenience.

The application of the RFA, in which the modal displacement takes the form $x(t) = A(t)\cos[\omega_1 t + \phi(t)]$, where $A(t)$ and $\phi(t)$ are slowly varying amplitude and phase envelopes, gives the following rotating-frame system:

$$\begin{cases} \dot{X} = \delta Y - \frac{3}{8}\alpha A^2 Y + \frac{1}{2}[F_2 \sin(\Theta) - \gamma X] \\ \dot{Y} = -\delta X + \frac{3}{8}\alpha A^2 X - \frac{1}{2}F_1 - \frac{1}{2}[F_2 \cos(\Theta) + \gamma Y] \\ \dot{\Theta} = \Omega = (\omega_2 - \omega_1)/\omega_0 \end{cases} \quad (2)$$

where $X = A\cos(\phi)$ and $Y = A\sin(\phi)$ are the rotating-frame quadratures, $A^2 = X^2 + Y^2$, and $\delta = (\omega_1 - \omega_0)/\omega_0$ (details are provided in the Supplemental Material [36]).

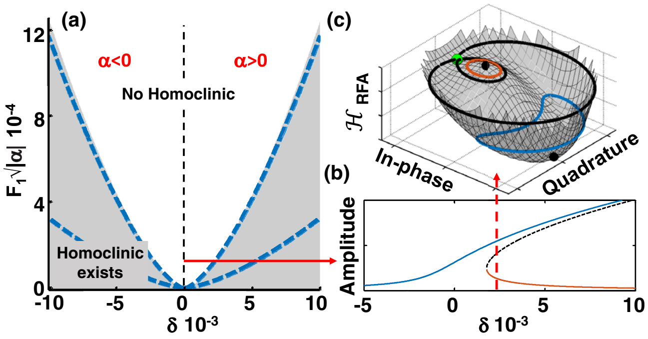

FIG. 1. (a) Bistability map plotted as a function of dimensionless force and detuning, showing the region of bistability for a lossless driven Duffing resonator (gray area), and for a low-loss ($Q = 1000$) Duffing resonator (area between the dashed blue lines). (b) Amplitude (arbitrary units) versus detuning response of a lossless Duffing taken for $F_1\sqrt{\alpha} = 10^{-4}$. The corresponding phase-space plot (also in arbitrary units) for a detuning of $\delta = 2.5 \times 10^{-3}$ is shown in (c). The stable fixed points and the saddle point are shown as black and green dots, respectively, and the black traces correspond to the homoclinic orbits. Small amplitude libration orbits around the high-amplitude branch (blue) and low-amplitude branch (red) are shown. α is the Duffing parameter.

Since Eqs. (1) and (2) are generically applicable to Duffing-type resonators, the results below can, in principle, be implemented in various physical realizations of nonlinear resonators, such as optical [37] and superconducting resonators [38], without loss of generality.

Initially, consider the conventional case with only one applied force, i.e., $F_2 = 0$, whereby the system in Eq. (2) is reduced to the first two equations only. The fixed points of the system, obtained by setting the time derivative in Eq. (2) to zero, exhibit a bistable response in a region of the dimensionless parameter space shown in Fig. 1(a) for a lossless and a low-loss ($\gamma = 10^{-3}$) driven Duffing resonators. To visualize the phase space and associated homoclinic orbits, we select a constant-force cut through the parameter space, Fig. 1(b), and then a constant-detuning cut where bistability exists, Fig. 1(c). It is convenient to plot the RFA Hamiltonian ($\mathcal{H}_{\text{RFA}}$) [39,40], shown in Fig. 1(c), along with the fixed points. For the case $\gamma = 0$, trajectories on the $\mathcal{H}_{\text{RFA}}$ surface follow closed orbits around the fixed points, the so-called libration orbits [41]. A homoclinic orbit is then the limit case in which the libration orbit intersects the saddle point, as shown in Fig. 1(c).

Note that for $F_2 = 0$ the system of Eq. (2) is reduced to an autonomous two-dimensional system ($n = 2$), which cannot generate chaos as it lacks the necessary dimensionality. However, an additional time dependence introduced by making $F_2 \neq 0$ increases the RFA dimensions from $n = 2$ to $n = 3$, thus in principle meeting the condition for chaos generation. Thus, by setting $F_2 \neq 0$ chaos could be generated if the homoclinic orbits are sufficiently perturbed. The introduction of higher-order perturbation terms in Eq. (2) could in principle induce chaos even for $F_2 = 0$.

However, any time dependence conferred by these higher-order terms only becomes significant near the homoclinics, i.e., the saddle-node bifurcation points.

The above arguments are corroborated by a combination of numerical simulations and measurements. The experiments are performed using a microbeam GaAs piezoelectric microelectromechanical systems resonator driven into the nonlinear Duffing regime, details regarding fabrication and basic properties of such resonators can be found in Ref. [42]. The resonator is placed in a vacuum chamber, and its motion is measured using a laser Doppler vibrometer, whose output is fed simultaneously to a lock-in amplifier and a vector signal analyzer (for experimental details, see the Supplemental Material [36]). A higher harmonic mode is selected for these experiments to avoid possible intermodal interactions [43,44].

The application of a single-tone sweep produces the frequency response shown in Fig. 2(a) for the linear (100 $\mathrm{mV_{PP}}$, black trace) and nonlinear Duffing regimes (3 $\mathrm{V_{PP}}$, red and blue traces), which, upon fitting, give the following values for the resonator parameters $\omega_0/2\pi = 1.56$ MHz, $Q = 1000$, and $\alpha = 1.67 \times 10^{15}$ $\mathrm{Hz/V^2}$.

As a first demonstration of the period-doubling route to chaos, a two-tone excitation is applied to the resonator with one fixed tone in the bistability region ($F_1 = 3$ $\mathrm{V_{PP}}$, $\omega_1/2\pi = 1566.5$ kHz) and one swept tone. For large detunings between the two tones, the rotating-frame response corresponds to a low-amplitude libration oscillation having a frequency Ω. As the tone is swept, the oscillations exhibit a quick succession of period-doubling bifurcations leading to chaos, as shown in Fig. 2(b) for both the high- and low-amplitude branches. The corresponding phase-space plots for period 1 ($P1$), period 2 ($P2$), and chaotic attractors are shown in Figs. 2(c)–2(e), respectively. Note that, as will be demonstrated later, Fig. 2(b) indicates that the low-amplitude branch only generates chaos for negative detuning, i.e., $\Omega < 0$, while the high-amplitude branch only generates chaos for $\Omega > 0$.

Making $F_2 \neq 0$ is clearly a necessary but not sufficient condition for chaos generation, and the question of whether and where in the four-dimensional parameter space (δ, Ω, F_1, and F_2) chaos exists remains to be addressed. While bounds have been set on the values of F_1 and δ such that bistability exists for $F_2 = 0$, similar bounds for F_2 and Ω have yet to be determined. This task is usually performed by applying Melnikov's method, which sets strict conditions for the period-doubling bifurcation route to chaos to take place [22–25,45–47].

Ideally, the application of Melnikov's method constrains chaos generation in parameter space with an analytical bound. Unfortunately, straightforward application of Melnikov's integral to the archetypal nonlinear resonator captured by Eq. (1) results in a relation that is not easily amenable to analytical solution. Therefore, in order to obtain a rough analytical bound, a heuristic approach analogous to the one employed in Ref. [23] is used. This approach considers that the application of a second forcing term creates the libration orbits, and the amplitude at which these libration orbits are large enough to undergo interwell jumps is considered to be a lower bound for the onset of period-doubling bifurcation. Provided that, if $|\Omega| \ll \gamma$ no chaos is generated [48], and if $|\Omega| \gg \gamma$ the RFA is no longer valid. By linearizing the libration orbit around the fixed point, an approximate closed-form bound

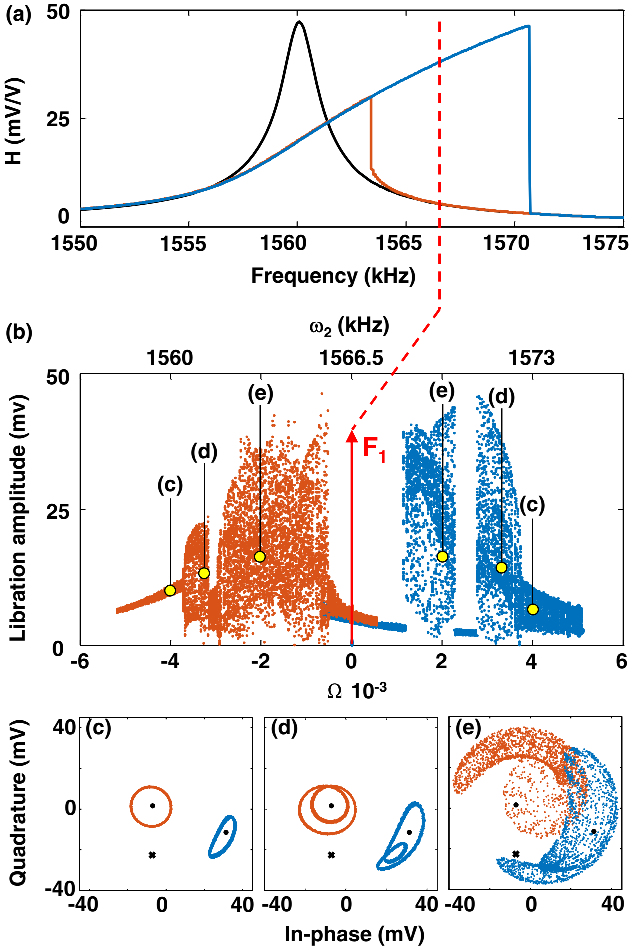

FIG. 2. (a) Experimental lock-in amplifier data for the frequency response obtained by a single tone sweep showing the linear (black trace 100 $\mathrm{mV_{PP}}$) and the Duffing regimes (3 $\mathrm{V_{PP}}$); the latter shows bistability upon performing a forward (blue trace) and a backward sweep (red trace). H denotes the relative amplitude response, expressed in mV per V drive. (b) Scatter plot of periodically sampled libration oscillation under the effect of a two-tone excitation, with one fixed tone (indicated by F_1 having $\omega_1/2\pi = 1566.5$ kHz and $F_1 = 3$ $\mathrm{V_{PP}}$) and one swept tone ($F_2 = 2.1$ $\mathrm{V_{PP}}$, 1558 kHz $< \omega_2/2\pi <$ 1576 kHz), shown for the lower (red) and higher (blue) amplitude branches. Period 1, period 2, and chaotic oscillations are detected and shown in (c)–(e), respectively, for both the high (blue) and low (red) amplitude branches. The black dots correspond to the experimentally-obtained fixed points, and the crosses correspond to the calculated saddle point.

for the period-doubling route to chaos can then be expressed as (see the Supplemental Material [36] for a detailed derivation):

$$F_{2C1,3} = \sqrt{4(\omega_L - \Omega)^2 + \gamma^2} \times |A_2 - A_{1,3}|, \qquad (3)$$

where F_{2C1} and F_{2C3} indicate the critical F_2 necessary to induce period doubling, ω_L is the libration frequency, and A_1, A_2, and A_3, are the amplitudes of the three steady-state fixed points, with A_1, A_3 as the stable ones, and A_2 being the unstable one. Setting $\Omega = \omega_L$ gives the minimum value of $F_{2C1,3}$ which we denote $\mathrm{F}_{2\ \mathrm{min}\ 1,3}$.

Equation (3) sheds light on the experimental results in Fig. 2: by realizing that $\omega_L < 0$ for the low-amplitude branch and $\omega_L > 0$ for the high-amplitude branch, it is easy to understand that period doubling in Fig. 2(b) takes place mostly for $\Omega \approx \omega_L$. This is further confirmed by looking at the basins of attraction, Fig. 3(a), where, depending on the value of Ω, only one of the two basins is strongly disturbed.

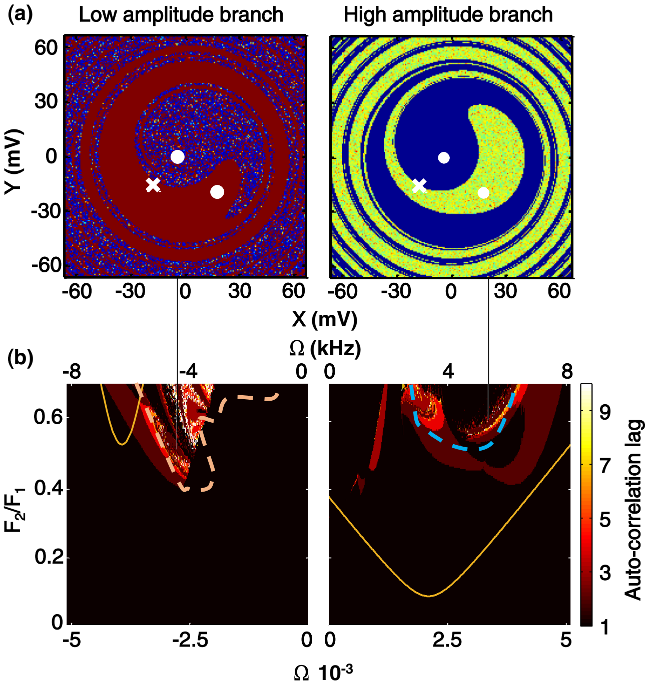

FIG. 3. Numerical simulations obtained for $\delta = 4.2 \times 10^{-3}$ (i.e., $\omega_1/2\pi = 1566.5$ kHz), and $F_1\sqrt{\alpha} = 1.5 \times 10^{-4}$ (i.e., $\mathrm{F}_1 = 3\ \mathrm{V_{PP}}$). (a) Basins of attraction under the effect of $F_2 = 0.6F_1$, $\Omega = 3.275 \times 10^{-3}$ for the high-branch, and $F_2 = 0.5F_1$, $\Omega = -2.7 \times 10^{-3}$ for the low-branch showing that only one of the two basins is disturbed depending on the value of Ω. The white dots and crosses mark the location of the stable and saddle points in the unperturbed system, respectively. (b) Two-dimensional maps (both panels) showing the location of autocorrelation peak as a function of detuning and forcing (Ω, F_2). Values greater than 1 (red and bright areas) indicate period-doubling bifurcations and chaos. The experimentally obtained bifurcation areas are equally shown (delineated by the dashed lines). The area bounded by the analytical model, i.e., F_{2C}, is shown as the solid yellow lines. The solid vertical lines indicate where in the (F_2, Ω) parameter space the basins in (a) are located.

A two-dimensional sweep of Ω and F_2 provides further grounds for comparison between the numerical, analytical, and experimental results. Such a sweep is shown in Fig. 3 for both solution amplitude branches and the same drive conditions as in Fig. 2, i.e., $\omega_1/2\pi = 1566.5$ kHz and $F_1 = 3\ \mathrm{V_{PP}}$. Figure 3 plots the lag of the autocorrelation maximum for the experimentally and numerically obtained time-domain signals, where an autocorrelation lag of 1 indicates $P1$ orbits, a lag of 2 indicates $P2$ orbits, and so on. Experimental and numerical data agree well in predicting the region corresponding to $P2$, the higher order bifurcations, and chaos. It is also interesting to note that both types of time-domain data show that for some parameter-space values interbranch jumps occur, where the system jumps from the vicinity of one fixed point to the other where it remains stuck in a low amplitude libration orbit. Chaos is verified for a selection of experimental traces, where a correlation dimension [49] of $D_2 = 2.2 \pm 0.1$ and $D_2 = 2.3 \pm 0.1$ is estimated for the high- and low-amplitudes branches, respectively. When a similar analysis is undertaken for simulated time series, the corresponding largest Lyapunov exponent calculated directly from the differential equations is $\lambda_1 = 0.141 \pm 0.002$ and $\lambda_1 = 0.131 \pm 0.002$ (see the Supplemental Material [36] and [50–57]).

Both results presented in Fig. 3 validate the main conclusions of the analytical model; for instance, the $P2$ bifurcation is mainly obtained with negative detuning for the low amplitude branch and positive detuning for the high amplitude branch, as predicted by the libration frequency analysis. Experimental and numerical results also demonstrate that the model can help constrain the necessary parameter space for chaos generation. It is equally interesting to note that the low-amplitude branch simulations have a well-formed wedge area for period doubling and chaos, and this is nearer to the analytically constrained parameter space compared to the high-amplitude branch. This can plausibly be attributed to the shape of the libration orbits around the low-amplitude branch, which more closely resembles circular ones compared to the almost banana-shaped high-amplitude branch libration orbits.

Next, we verify how closely the analytical and numerical results evolve as a function of changing drive conditions (changing δ or F_1). Based on the analytical model, it would be expected that, as the edge of the bistable area is approached, the distance between one of the stable fixed points and the unstable fixed point shrinks to zero, and as a consequence, the necessary F_2 required to achieve $P2$ and chaos itself is reduced to zero. This is confirmed numerically by performing 3D sweeps (δ, Ω, and F_2) and tracking the minimum necessary values of F_2 and Ω for the onset of $P2$. These are plotted against δ (for $F_1 = 3\ \mathrm{V_{PP}}$), along with $F_{2\ \mathrm{min}}$ and Ω_{min} as obtained from Eq. (3), in Figs. 4(b)

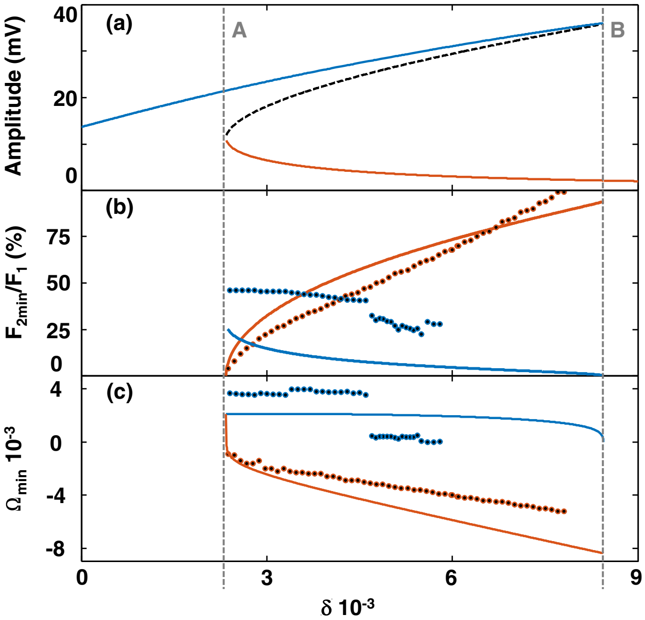

FIG. 4. Comparison between numerical (dots) and analytical (solid lines) values of $F_{2\,\min}$ (b) and $\Omega_{\min}$ (c) required for $P2$ and chaos for both the low amplitude branch (red) and high amplitude branch (blue) of the Duffing resonator shown in (a). For both numerical and analytical data, $P2$ only appears in the range where bistability exists (indicated by the dashed vertical gray lines, and denoted A and B, respectively). As the high amplitude branch approaches the saddle-node bifurcation its libration motion becomes more unstable, hence the data points do not reach the saddle-node bifurcation.

and 4(c), respectively. Again, numerical results agree with the main features of the analytical model, in that both F_2 and Ω reduce to zero as the saddle node bifurcation is approached. Similarly to the results in Fig. (3), the analytical results for the low-amplitude branch adhere better to the numerical simulations compared to the high-amplitude branch ones, which show more exotic dynamics, a repeated hint that the eccentric libration orbit is more difficult to model.

It is interesting to ask whether the perturbed homoclinic-based argument presented above remains valid for the region where bistability is suppressed by the damping (note that the Melnikov approach requires bistability in the lossless version of the system). Indeed, the Melnikov method requires a homoclinic in the undamped system; however, it also assumes that the additional damping and forcing [corresponding to the terms within the brackets in Eq. (2)] are small, perturbationlike terms. The authors therefore conjecture that, in the case of suppressed bistability, these terms are sufficiently large to invalidate the perturbed Hamiltonian approach.

On a practical note, it maybe tempting to pursue chaos generation by positioning the drive near the saddle-node bifurcation, as that would require a very small perturbation tone. This, however, is not an optimal experimental condition as it would be easy under the effect of noise to jump to the adjacent potential well and remain stuck there in a low-amplitude libration orbit. It is therefore more favourable for practical ends to position the main tone towards the middle of the bistable region and apply a moderate-amplitude second tone.

In summary, this Letter presented an approach to chaos generation in nonlinear MNEMS resonators that uses drive amplitudes that are smaller than those previously reported. The method relies on applying two drive tones in order to make the rotating-frame phase-space three dimensional, and presents a model that uses linearization of perturbations within the rotating frame to constrain the parameter space where chaos can be generated. This approach demonstrates that once bistability has been accessed via the first applied tone, chaos can be generated using a lower amplitude perturbing second tone. The generality of the proposed method, and the relatively low driving forces involved underline applicability to a large range of nonlinear resonators thus potentially placing resonators, particularly MNEMS ones, as leading candidates for the high-integration physical implementation of networks and reservoirs, as well as the experimental investigation of chaos-related phenomena.

This work is partly supported by a MEXT Grant-in-Aid for Scientific Research on Innovative Areas Science of hybrid quantum systems (Grants No. JP15H05869 and No. JP15K21727). The work of Ludovico Minati was supported by the World Research Hub Initiative (WRHI), Institute of Innovative Research (IIR), Tokyo Institute of Technology, Tokyo, Japan.

---

[*] Samer.Houri.dg@hco.ntt.co.jp
[†] minati.l.aa@m.titech.ac.jp

[1] R. C. Hilborn *et al.*, *Chaos and Nonlinear Dynamics: An Introduction for Scientists and Engineers* (Oxford University Press, Oxford, 2000).
[2] E. Ott, *Chaos in Dynamical Systems* (Cambridge University Press, Cambridge, England, 2002).
[3] A. Buscarino, L. Fortuna, M. Frasca, G. Sciuto *et al.*, *A Concise Guide to Chaotic Electronic Circuits* (Springer, New York, 2014).
[4] S. Boccaletti, A. N. Pisarchik, C. I. Del Genio, and A. Amann, *Synchronization: From Coupled Systems to Complex Networks* (Cambridge University Press, Cambridge, England, 2018).
[5] L. Minati, Acta Phys. Pol. B **49**, 2029 (2018).
[6] G. Tanaka, T. Yamane, J. B. Héroux, R. Nakane, N. Kanazawa, S. Takeda, H. Numata, D. Nakano, and A. Hirose, Neural Networks **115**, 100 (2019).
[7] R. Lifshitz and M. Cross, Rev. Nonlinear Dyn. Complexity **1**, 1 (2008).
[8] M. I. Younis, E. M. Abdel-Rahman, and A. Nayfeh, J. Microelectromech. Syst. **12**, 672 (2003).

[9] J. Güttinger, A. Noury, P. Weber, A. M. Eriksson, C. Lagoin, J. Moser, C. Eichler, A. Wallraff, A. Isacsson, and A. Bachtold, Nat. Nanotechnol. **12**, 631 (2017).

[10] R. B. Karabalin, M. C. Cross, and M. L. Roukes, Phys. Rev. B **79**, 165309 (2009).

[11] E. Kenig, Y. A. Tsarin, and R. Lifshitz, Phys. Rev. E **84**, 016212 (2011).

[12] J. Bienstman, J. Vandewalle, and R. Puers, Sens. Actuators, A **66**, 40 (1998).

[13] M. Ashhab, M. Salapaka, M. Dahleh, and I. Mezić, Nonlinear Dyn. **20**, 197 (1999).

[14] K. Park, Q. Chen, and Y.-C. Lai, Phys. Rev. E **77**, 026210 (2008).

[15] S. K. De and N. R. Aluru, J. Microelectromech. Syst. **15**, 355 (2006).

[16] Y. C. Wang, S. G. Adams, J. S. Thorp, N. C. MacDonald, P. Hartwell, and F. Bertsch, IEEE Trans. Circuits Syst. I **45**, 1013 (1998).

[17] B. E. DeMartini, H. E. Butterfield, J. Moehlis, and K. L. Turner, J. Microelectromech. Syst. **16**, 1314 (2007).

[18] S. Towfighian, G. Heppler, and E. Abdel-Rahman, J. Comp. Nonlin. Dyn. **6**, 011001 (2011).

[19] D. V. Scheible, A. Erbe, R. H. Blick, and G. Corso, Appl. Phys. Lett. **81**, 1884 (2002).

[20] S. A. Emam and A. H. Nayfeh, Nonlinear Dyn. **35**, 1 (2004).

[21] R. Abraham and Y. Ueda, The Chaos Avant-garde: Memories of the Early Days of Chaos Theory (World Scientific, Singapore, 2000).

[22] A. Sharma, V. Patidar, G. Purohit, and K. Sud, Commun. Nonlinear Sci. Numer. Simul. **17**, 2254 (2012).

[23] F. C. Moon, J. Appl. Mech. **47**, 638 (1980).

[24] P. Holmes, Phil. Trans. R. Soc. A **292**, 419 (1979).

[25] F. Moon and P. J. Holmes, J. Sound Vib. **65**, 275 (1979).

[26] V. Kaajakari, T. Mattila, A. Oja, and H. Seppa, J. Microelectromech. Syst. **13**, 715 (2004).

[27] A. N. Cleland, *Foundations of Nanomechanics: From Solid-State Theory to Device Applications* (Springer Science & Business Media, Berlin, 2013).

[28] A. H. Nayfeh and D. T. Mook, *Nonlinear oscillations* (Wiley Classics Library, Hoboken, 1980).

[29] B. Charlot, W. Sun, K. Yamashita, H. Fujita, and H. Toshiyoshi, J. Micromech. Microeng. **18**, 045005 (2008).

[30] G. M. Bernstein and M. A. Lieberman, IEEE Trans. Comput.-Aided Des. Integr. Circuits Syst. **37**, 1157 (1990).

[31] K. Yagasaki, J. Sound Vib. **183**, 1 (1995).

[32] D. S. Greywall, B. Yurke, P. A. Busch, A. N. Pargellis, and R. L. Willett, Phys. Rev. Lett. **72**, 2992 (1994).

[33] I. Kozinsky, H. W. C. Postma, O. Kogan, A. Husain, and M. L. Roukes, Phys. Rev. Lett. **99**, 207201 (2007).

[34] I. Kozinsky, H. C. Postma, I. Bargatin, and M. Roukes, Appl. Phys. Lett. **88**, 253101 (2006).

[35] V. K. Mel'nikov, Tr. Mosk. Mat. Obs. **12**, 3 (1963).

[36] See the Supplemental Material at http://link.aps.org/supplemental/10.1103/PhysRevLett.125.174301 for experimental setup, additional calculations, and non-linear time-series analysis.

[37] T. Hansson and S. Wabnitz, Phys. Rev. A **90**, 013811 (2014).

[38] V. E. Manucharyan, E. Boaknin, M. Metcalfe, R. Vijay, I. Siddiqi, and M. Devoret, Phys. Rev. B **76**, 014524 (2007).

[39] M. I. Dykman, G. Rastelli, M. L. Roukes, and E. M. Weig, Phys. Rev. Lett. **122**, 254301 (2019).

[40] J. S. Huber, G. Rastelli, M. J. Seitner, J. Kölbl, W. Belzig, M. I. Dykman, and E. M. Weig, Phys. Rev. X **10**, 021066 (2020).

[41] S. Houri, D. Hatanaka, M. Asano, and H. Yamaguchi (unpublished).

[42] H. Yamaguchi, Semicond. Sci. Technol. **32**, 103003 (2017).

[43] S. Houri, D. Hatanaka, M. Asano, and H. Yamaguchi, Phys. Rev. Applied **13**, 014049 (2020).

[44] S. Houri, D. Hatanaka, M. Asano, R. Ohta, and H. Yamaguchi, Appl. Phys. Lett. **114**, 103103 (2019).

[45] F. C. Moon, Phys. Rev. Lett. **53**, 962 (1984).

[46] F. C. Moon and G.-X. Li, Phys. Rev. Lett. **55**, 1439 (1985).

[47] J. A. Sanders, Celest. Mech. **28**, 171 (1982).

[48] S. Houri, R. Ohta, M. Asano, Y. M. Blanter, and H. Yamaguchi, Jpn. J. Appl. Phys. **58**, SBBI05 (2019).

[49] R. Hegger, H. Kantz, and T. Schreiber, Chaos **9**, 413 (1999).

[50] A. Wolf, J. B. Swift, H. L. Swinney, and J. A. Vastano, Physica (Amsterdam) **16D**, 285 (1985).

[51] A. M. Fraser and H. L. Swinney, Phys. Rev. A **33**, 1134 (1986).

[52] T. Sauer, J. A. Yorke, and M. Casdagli, J. Stat. Phys. **65**, 579 (1991).

[53] A. Provenzale, L. A. Smith, R. Vio, and G. Murante, Physica (Amsterdam) **58D**, 31 (1992).

[54] P. Grassberger and I. Procaccia *et al.*, Physica (Amsterdam) **9D**, 189 (1983).

[55] L. Minati, Chaos **24**, 033110 (2014).

[56] M. Riedl, A. Müller, and N. Wessel, Eur. Phys. J. Spec. Top. **222**, 249 (2013).

[57] C. Bandt and B. Pompe, Phys. Rev. Lett. **88**, 174102 (2002).